

## THE M SUPERGIANT HIGH MASS X-RAY BINARY 4U 1954+31

KENNETH H. HINKLE <sup>1</sup>, THOMAS LEBZELTER <sup>2</sup>, FRANCIS C. FEKEL <sup>3</sup>,  
OSCAR STRANIERO <sup>4</sup>, RICHARD R. JOYCE <sup>1</sup>, LISA PRATO <sup>5</sup>,  
NICOLE KARNATH <sup>6</sup> AND NOLAN HABEL <sup>7</sup>

<sup>1</sup>*NSF's National Optical-Infrared Astronomy Research Laboratory,  
P.O. Box 26732, Tucson, AZ 85726, USA*

<sup>2</sup>*Department of Astrophysics, University of Vienna, Türkenschanzstrasse 17, 1180 Vienna, Austria*

<sup>3</sup>*Tennessee State University, Center of Excellence in Information Systems,  
3500 John A. Merritt Boulevard, Box 9501, Nashville, TN 37209, USA*

<sup>4</sup>*INAF, Osservatorio Astronomico d'Abruzzo,  
I-64100 Teramo, Italy, and INFN-LNGS, Assergi (AQ), Italy*

<sup>5</sup>*Lowell Observatory, 1400 W. Mars Hill Rd, Flagstaff, AZ 86001, USA*

<sup>6</sup>*SOFIA-USRA, NASA Ames Research Center, MS 232-12, Moffett Field, CA 94035, USA*

<sup>7</sup>*University of Toledo, Department of Physics and Astronomy,  
2801 West Bancroft Street, Toledo, Ohio 43606 USA*

### ABSTRACT

The X-ray binary 4U 1954+31 has been classified as a Low Mass X-ray Binary (LMXB) containing a M giant and a neutron star (NS). It has also been included in the rare class of X-ray symbiotic binaries (SyXB). The Gaia parallax, infrared colors, spectral type, abundances, and orbital properties of the M star demonstrate that the cool star in this system is not a low mass giant but a high mass M supergiant. Thus, 4U 1954+31 is a High Mass X-ray Binary (HMXB) containing a late-type supergiant. It is the only known binary system of this type. The mass of the M I is  $9_{-2}^{+6} M_{\odot}$  giving an age of this system in the range 12 – 50 Myr with the NS no more than 43 Myr old. The spin period of the NS is one of the longest known, 5 hours. The existence of M I plus NS binary systems is in accord with stellar evolution theory, with this system a more evolved member of the HMXB population.

*Keywords:* stars: abundances — stars: evolution — stars: individual (4U 1954+31) — stars: late-type — X-rays: binaries

### 1. INTRODUCTION

X-ray binaries consist of a neutron star (NS) or black hole (BH) accreting material from a companion star. The class of X-ray binaries is divided into Low Mass X-ray binaries (LMXB) and High Mass X-ray binaries (HMXB) (see review by [Tauris & van den Heuvel 2006](#)). The companion star to the NS in the LMXB systems is old,  $>10^9$  yr, with spectral type later than B and mass less than  $2 M_{\odot}$ .

The LMXB are further divided into two classes, low-luminosity dwarf – NS systems and a rare group of late-type giant – NS systems (Liu et al. 2007). The late-type giant – NS systems are also classified as Symbiotic X-ray binaries (SyXB, Mürset et al. 1997). HMXB consist of a massive, young star, with initial mass  $\gtrsim 8 M_{\odot}$ , plus a NS (Sander 2018). In HMXB three classes of companion stars are known, main sequence (MS) Be stars, supergiant O and B stars, and Roche-lobe filling early-type supergiants (Chaty 2011). These various groups, of course, describe the systems with longer lifetimes or more common evolutionary paths and do not cover all the evolutionary products possible (Tauris & van den Heuvel 2006; Yungelson et al. 2019).

Symbiotic binaries, labelled SySt, are one of the several varieties of wide binary systems consisting of an evolved star plus a degenerate object (Escorza et al. 2020). SySt consist of a white dwarf (WD) accreting mass from, typically, a K or M giant. These objects are characterized by optical spectra with absorption features of a late-type giant combined with a high excitation emission-line spectrum (Merrill 1958; Kenyon & Webbink 1984). There is one late-type star – NS binary, V2116 Oph, that is generally included in the SySt group. The SyXB are an unusual subset of the SySt, since most have nearly normal optical spectra. SyXB are first identified as X-ray sources and then later associated with M-type optical counterparts. Since the companion star to the NS in this group of LMXB is a giant, the orbital periods are measured in years, rather than hours as is the case for LMXB with dwarf companions.

To date, the total number of confirmed SyXB systems is barely over a half dozen with the Galactic population estimated to be  $\sim 100$ – $1000$  (Lü et al. 2012; Yungelson et al. 2019). Two SyXB have well determined orbits, V2116 Oph=GX1+4 (Hinkle et al. 2006) and V934 Her=4U 1700+24 (Hinkle et al. 2019), with orbital periods of 3.2 and 12.0 years, respectively. The stellar companion to the NS is, in both cases, a M III with a mass around  $1.5 M_{\odot}$ . The NS spin in the SyXB binaries is exceedingly slow with a period of minutes to hours (Lü et al. 2012; Enoto et al. 2014). Radio pulsars all show much shorter spin periods (Tauris & van den Heuvel 2006). Very slow pulsars, like those discussed here, are detected in the X-ray only.

To further explore the SyXB class we focus here on 4U 1954+31. 4U 1954+31 is a reasonably bright,  $V=10$  and  $K=3.5$ , northern M star. This star was included in a survey of SyXB systems that we are undertaking. Gaia data revealed it to be overly luminous for a giant. We review below multiple lines of evidence that show this M star, the late-type companion of the NS in the 4U 1954+31 binary, to be a massive late-type supergiant. The supergiant is the evolutionary product of a B star, i.e. the system is a more evolved HMXB. The existence of such an object is not surprising (Nebot Gómez-Morán et al. 2015), although not widely discussed in the X-ray binary literature. The possibility that the SyXB system Sct X-1 contains a supergiant was discussed by Kaplan et al. (2007) but this has not been confirmed; Gaia data release 2 does not include a parallax for Sct X-1. In the following sections we review the literature on 4U 1954+31, derive the parameters for the supergiant, analyze the surface abundances, and discuss the evolution of this system.

## 2. A BRIEF REVIEW OF 4U 1954+31

4U 1954+31<sup>1</sup> was first detected by *Uhuru* (Forman et al. 1978). Masetti et al. (2007), Corbet et al. (2008) and Enoto et al. (2014) review the detections by subsequent surveys. The position

<sup>1</sup> Some of the X-ray literature uses the alias WISEA J195542.33+320548.8 for 4U 1954+31. This is not a recognized alias in Simbad.

derived from early X-ray surveys was uncertain and identification with several stars was possible, including a Be star (Tweedy et al. 1989). *Chandra* significantly decreased the uncertainty in the X-ray position and resulted in a positional identification with a M star (Masetti et al. 2006). The positions are consistent at the  $1.8\sigma$  level and the identification considered secure. From a R ( $\lambda/\Delta\lambda$ )  $\sim 800$  spectrum in the red the stellar spectral type was found to be a M4–5 III and 4U 1954+31 classified as an LMXB SyXB (Masetti et al. 2006). It appears as a LMXB in the compilation of Boodaghee et al. (2007). A distance of 1.7 kpc was determined by using an absolute magnitude for a M 4 III combined with the observed *V* and *R* magnitudes. Masetti et al. (2006) note that this is an upper limit to the distance because interstellar reddening had not been taken into account.

*Swift/BAT* data revealed a  $\sim 5$  hour periodicity. Mattana et al. (2006) argued that the 5 hr periodicity is incompatible with orbital motion for reasonable NS and M III masses and separations. Taking the period as the NS spin period, 4U 1954+31 is one of the slowest known pulsars. If the NS is rotating at the equilibrium period for disk accretion, the pulsar period implies a magnetic field strength of  $\sim 10^{15}$  G (Corbet et al. 2006, 2008).

Standard masses and the absence of evidence of mass exchange from a contact or CE binary implies a lower limit of the orbital period of  $\sim 400$  days. This agrees with the absence of eclipses in the X-ray data. The large size of the M III and the absence of eclipses requires either a highly inclined orbit or a long orbital period (Masetti et al. 2007).

Several papers also note connections between 4U 1954+31 and HMXB systems. Both the shape of the 4U 1954+31 X-ray spectrum and the observed X-ray flaring are in agreement with classification as a HMXB (Masetti et al. 2006). 4U 1954+31 is star number 475 of the INTEGRAL/IBIS hard X-ray survey and cataloged as a HMXB (Krivonos et al. 2010). It also is listed in the BAT all-sky hard X-ray survey (Baumgartner et al. 2013) and the IBIS soft gamma-ray survey (Bird et al. 2016). Marcu et al. (2011) measured the NS spin period at 5.3 hr and variable with both spin-up and spin-down which has parallels in HMXB systems. Enoto et al. (2014) discuss extensive *Suzaku*, *Swift/BAT*, and *RXTE/ASM* observations of 4U 1954+31. They found a 5.4 hr NS spin period with  $\sim 7\%$  variations, similar to slowly rotating pulsars in HMXB. They conclude that quasi-spherical, subsonic accretion onto the NS is a plausible explanation of the data. They assume a  $\sim 10^{13}$  G field for the NS. Recurring irregular flares during outbursts with a typical timescale of  $\sim 50$  s were interpreted as intermittent accretion from the Alfvén radius. Masetti et al. (2007) and Enoto et al. (2014) detected a narrow Fe-K $\alpha$  line at 6.4 keV, a characteristic of NS in HMXB.

### 3. NEW OBSERVATIONS AND REDUCTIONS

Our observational data draw from two sources, a high-resolution near-IR spectrum obtained with the Immersion Grating Infrared Spectrometer (IGRINS, Park et al. 2014) at the Lowell Discovery Telescope (LDT) and a time series of optical high-resolution spectra taken with the Tennessee State University 2 m Automatic Spectroscopic Telescope (AST) and fiber fed echelle spectrograph (Eaton & Williamson 2007).

The IGRINS/LDT spectrum was observed on 2018 Nov 23. The spectrum covers the *H* and *K* region at R=45000. The reductions follow those of other SyXB spectra observed with IGRINS on the Gemini South Telescope (Hinkle et al. 2019). The initial reduction was done using the IGRINS pipeline. The output from this process are the echelle orders which have been ratioed to a telluric reference standard. The continuum in each order was removed with a linear fit to the high points. The higher order polynomial terms in the continuum were removed with the IRAF continuum routine

*splot 't'* at low order. The orders were joined by matching the overlap regions between the orders. The velocities of the *H*-band CO second overtone lines were measured and this velocity is listed in Table 1.

From 2017 October through 2020 June we observed the spectrum of 4U 1954+31 with the Tennessee State University 2 m Automatic Spectroscopic Telescope (AST) and Fiber-Fed Echelle Spectrograph (FFES, Eaton & Williamson 2007). For these observations the detector was a Fairchild 486 CCD that has a  $4096 \times 4096$  array of  $15 \mu\text{m}$  pixels (Fekel et al. 2013). The spectra were acquired with a fiber that results in a resolving power of 25000 at  $6000 \text{ \AA}$  and contain 48 orders that range from 3800 to  $8260 \text{ \AA}$ . Unfortunately, the S/N of these spectra is insufficient for abundance analysis. The observations are listed in Table 1 and were used for velocities.

An overview of the velocity reductions for the AST data can be found in Fekel et al. (2009). For 4U 1954+31 a set of 40 lines were used that range in wavelength from  $5000 \text{ \AA}$  to  $6800 \text{ \AA}$ . These lines were selected from a more extensive solar-type star line list based on the line being relatively unblended in M-giant spectra. Zero point error in the AST data (Fekel et al. 2013) was corrected by comparing unpublished radial velocities of IAU radial velocity standards, measured from 2 m AST spectra, with the mean values of the same stars published in Scarfe et al. (1990). This indicated that the AST data needed a velocity correction of  $0.6 \text{ km s}^{-1}$  and this was applied to each of our AST velocities.

## 4. STELLAR AND BINARY SYSTEM PARAMETERS

### 4.1. *Effective Temperature, Luminosity, Radius, and Mass*

Masetti et al. (2006) found a spectral type for 4U 1954+31 of M4–5 III. However, comparison of the Gaia (Gaia Collaboration 2018) distance,  $3295^{+985}_{-631} \text{ pc}$  (Bailer-Jones et al. 2018), and the optical/near-IR magnitudes of 4U 1954+31 implies that the M star is much more luminous than a giant. The high resolution IGRINS spectrum was convolved to a resolution  $R = 3000$  and compared with K band standard star spectra of Wallace & Hinkle (1997). As shown in Figure 1 the spectrum matches that of a M4 supergiant and does not match a M4 giant.

To quantify this result the effective temperature was determined by an analysis of the near-IR spectra. Using the technique discussed by Hinkle et al. (2016), the H band second overtone vibration-rotation CO lines were measured. Over 100 minimally blended, moderately weak lines were identified and the CO excitation temperature,  $3200 \pm 100 \text{ K}$ , was found using curve-of-growth techniques. From Figure 1 of Lebzelter et al. (2019) the corresponding effective temperature is  $3340 \pm 240 \text{ K}$ . The Lebzelter et al. (2019) calibration of CO excitation temperature versus effective temperature employs M III stars. The calibration for M supergiants was confirmed by measuring the CO excitation temperature for  $\alpha$  Ori and  $\alpha$  Her using archival FTS data from the 4 m FTS (Pilachowski et al. 2017). The 4U 1954+31 CO excitation temperature of  $3200 \text{ K}$  is bracketed by the  $3300 \text{ K}$  value for the M2 Ia star  $\alpha$  Ori and the  $3150 \text{ K}$  value for the M 5 Ib–II star  $\alpha$  Her. Using the calibration of Lebzelter et al. (2019) these convert to effective temperatures of  $3590 \text{ K}$  for alpha Ori, and  $3220 \text{ K}$  for alpha Her, in agreement with their spectral types (M2 Ia and M5 Ib–II). The spectral type - effective temperature calibration of Levesque et al. (2005) gives an effective temperature of a M4 I as  $3535 \text{ K}$ , within our uncertainty.

Using literature photometry a spectral energy distribution (SED) for 4U 1954+31 was developed (Figure 2). From the compilation of Schlafly & Finkbeiner (2011) the visual extinction along the

line of sight toward 4U 1954+31 is  $A_v = 4.48$ . In Figure 2 a 3400 K blackbody is compared to the photometry dereddened by  $(V-K)_0=4.0$ . Averaging the various estimates for the effective temperature we adopt  $3450^{+100}_{-50}$  K. A 3450 K blackbody at the  $3295^{+985}_{-631}$  pc Gaia distance corresponds to a stellar radius of  $586^{+188}_{-127}$   $R_\odot$ . The luminosity is  $43880^{+34070}_{-15900}$   $L_\odot$ .

Figure 3 compares the position of the M4 I component of 4U 1954+31 in the HR diagram with standard evolutionary tracks for 7, 9, 11, 13, and 15  $M_\odot$  stars from non-interacting and non-rotating FuNS<sup>2</sup> evolutionary models (Straniero et al. 2019). All the tracks in Figure 3 refer to solar composition models. As appropriate for red supergiants, advanced evolution beyond the H and He burning phase was included. Accordingly, our tracks with  $M \geq 10 M_\odot$  follow the classical evolution of massive stars: H, He, C, Ne, O and Si burnings. Computations have been stopped after the Si burning phase, at the onset of the full nuclear statistical equilibrium (NSE), briefly before the core collapse. On the contrary, after the core-He burning, the 7 and 9  $M_\odot$  models undergo a degenerate C burning, at the end of which they experience a super-AGB phase. In this case, the computations have been stopped after a few thermal pulses. Note that the luminosity increases at the beginning of the super-AGB phase because of the occurrence of the hot bottom burning (Doherty et al. 2014). This phenomenon is stronger in the 9  $M_\odot$  model. The luminosity and effective temperature of 4U 1954+31 compared to the evolutionary tracks shows that the most likely mass is 9  $M_\odot$ . Uncertainty brackets masses of 7 to 15  $M_\odot$ . The corresponding surface gravity is 0.6 - 0.8  $\text{cm s}^{-2}$ , i.e.  $\log g \sim -0.15$ . Table 2 summarizes the stellar parameters derived for 4U 1954+31.

#### 4.2. Abundances

Abundances were measured using the spectral synthesis technique applied to the near-infrared IGRINS spectrum. As noted in section 3, the spectra in the visual range were not usable for such an analysis. Hydrostatic atmospheres from the COMARCS grid of models by Aringer et al. (2016) were employed and the spectra computed with the help of the COMA code (Aringer et al. 2016, and references therein). For the molecular lines of CO, CN, and OH the line list of Li et al. (2015) was selected with some modifications of line positions based on the Arcturus atlas (Hinkle et al. 1995), Brooke et al. (2014), and HITRAN08<sup>3</sup>, respectively. A standard model mass of 10  $M_\odot$  was used for all model calculations.

For the synthesis of the 4U 1954+31 model atmospheres were selected with  $T_{eff}=3400$  K and 3500 K and  $\log g=0.0$  and  $-0.5$  from the COMARCS grid to match the derived stellar parameters (Table 2). The microturbulence velocity was set to  $3 \text{ km s}^{-1}$ . This value has been used for  $\alpha$  Ori and a variety of other supergiants (e.g. Carr et al. 2000). The microturbulence was tested by using a macroturbulence velocity of  $4 \text{ km s}^{-1}$  to model a few unblended atomic lines. Molecular lines are hardly affected by the exact value of the microturbulence. Test calculations were also done altering the microturbulence to  $2.5 \text{ km s}^{-1}$ . The small deviation found was included in the uncertainties. As a starting point a solar composition was assumed. Beside the factors mentioned above, the setting of the continuum and line-by-line differences are included in the error budget. Non-LTE effects have not been taken into account.

The observed spectral region is extensive and practical limitations resulted in fitting sub-sections of the spectrum. Sets of lines for each studied element were used to guide the determination of the

<sup>2</sup> Software: Full Network Stellar (Straniero et al. 2006).

<sup>3</sup> <https://hitran.org>

abundance (Tables 3 and 4). For instance, for CO, we combined an overall fit to the  $\Delta v=3$  band heads listed in Table 4 with fits of individual lines in the H- and K-band. The line selection took into account the extent and quality of telluric correction at the corresponding wavelength, the presence of blending features, the general quality of the model fit in the surrounding parts of the spectrum, and in the case of the molecular lines, coverage of a broad range of transition bands and excitation levels. Papers by Carr et al. (2000) and Smith et al. (2013) were used as a starting point for the line selection. Identifications and positions were taken from the Arcturus atlas.

Abundances of the key elements C, N, and O were derived by altering each abundance until a simultaneous fit of the lines of CO, CN, and OH was achieved. The abundances of other elements were determined by choosing for each line the best fitting model from a small grid altering the abundances in steps of 0.05 dex. The elemental abundance was then computed as the mean from all lines considered. Changing the model temperature by up to 100 K resulted in a very small change in the line depths and thus the derived abundances. The abundances were more sensitive to  $\log g$ . Changing  $\log g$  from 0.0 to -0.5 leads to a strengthening of the atomic lines and as a consequence a systematic decrease of the abundances by typically 0.1 dex.

As a test, a high-resolution H- and K-band spectrum of  $\alpha$  Ori from the Kitt Peak FTS archive was synthesized. Using a data set extending from the near- into the thermal-IR, Lambert et al. (1984) derived  $[C/Fe]=-0.4$ ,  $[N/Fe]=+0.6$ , and  $[O/Fe]=-0.2$  for this star with typical uncertainties of 0.15 dex. The  $\alpha$  Ori stellar parameters of Lambert et al. (1984),  $T_{\text{eff}}=3800$  K,  $\log g=0.0$ , and microturbulence  $\xi=3$  km s $^{-1}$ , were selected for the test. The Lambert et al. (1984) carbon and nitrogen abundances were reproduced within the error bars although a slightly higher oxygen abundance was found. This likely results from the use by Lambert et al. (1984) of OH  $\Delta v=1$  lines that lie outside the H and K windows.

$^{12}\text{CO}$  lines in the 4U 1954+31 spectrum with central depths exceeding 60% could not be fit by our model spectra. This phenomenon is well known for the K-band spectra of highly evolved stars and likely indicates limitations of the atmospheric structure of the hydrostatic models (Lebzelter et al. 2019). Such lines were not included in our abundance analysis. We found that CN lines in the H-band give tentatively lower abundances of N than in the K-band. Since more isolated lines were accessible in the K-band than the H-band, we decided to put a higher weight on the results from the K-band.

Table 5 lists abundances obtained from the spectra for  $T_{\text{eff}} = 3400$  K and  $\log g = 0.0$ . 4U 1934+31 is slightly metal poor. The mean of the Ti and Fe abundance, elements represented by a good sample of lines, gives  $[M/H]=-0.33$ . An overabundance was found for Sc and Mn (average +0.25). Using a selection of  $^{13}\text{CO}$  lines the  $^{12}\text{C}/^{13}\text{C}$  ratio was determined by spectrum synthesis to be  $8\pm 2$ . Using the semi-empirical analysis of (Hinkle et al. 2016) the  $^{12}\text{C}/^{13}\text{C}$  was found to be  $9\pm 2$ , in agreement with the synthesis. For the oxygen isotopes,  $^{16}\text{O}/^{17}\text{O} = 2000_{-600}^{+1000}$  and  $^{16}\text{O}/^{18}\text{O} = 1400$  (single line).

### 4.3. Orbit

The goal of the velocity monitoring was to determine a single-lined spectroscopic orbit that would further constrain the physical properties of the system<sup>4</sup>. Velocities from AST are shown in Figure 4. After 2.5 years of monitoring, orbital motion is clearly present but the velocities have not yet closed.

<sup>4</sup> The convention concerning primary and secondary in this system can be confusing since we discuss both initial and final masses. The terms primary and secondary are used only where the meaning is unambiguous.

From the velocities three conclusions are apparent. The period of the orbit is  $\gtrsim 3$  yrs, the orbit is eccentric, and the systemic ( $\gamma$ ) velocity is  $\sim 4$  km s $^{-1}$ .

Systems that fill their Roche lobes undergo rapid mass transfer and, possibly, a common envelope episode. This is clearly not the case for 4U 1954+31, so that the radius of the supergiant must be smaller than the corresponding Roche lobe. The Roche lobe radius of the M star ( $R_L$ ) is governed by the mass ratio,  $q=M_{MI}/M_{NS}$ , and related to the binary separation,  $a$ , by:

$$\frac{R_L}{a} = \frac{0.49q^{\frac{2}{3}}}{0.6q^{\frac{2}{3}} + \ln(1 + q^{\frac{1}{3}})} \quad (1)$$

(Eggleton 1983). Assuming a typical neutron star mass of  $1.4 M_{\odot}$  and a mass of  $9 M_{\odot}$  for the M supergiant, the condition that  $R_L$  is larger than the estimated stellar radius, i.e.,  $590 R_{\odot}$  (Table 2), implies a minimum value for the binary separation of  $a \approx 1090 R_{\odot}$  ( $\sim 5$  AU). Then, Kepler's third law gives a minimum orbital period of 3.55 yrs. The current observations limit the orbital period to  $\gtrsim 3$  yrs corresponding to a binary separation  $\gtrsim 4.8$  AU, in agreement with the supergiant nature of the M star. For instance, with a 3 yr period and the Roche lobe greater than the estimated stellar radius, the supergiant mass should be  $\leq 11.6 M_{\odot}$ . However, a longer period would allow even higher masses.

In principle, the Corbet diagram could provide an empirical relation between the spin period and orbital period (Knigge et al. 2011; Enoto et al. 2014). However, the spin period of 4U 1934+31 is among the longest known and the Corbet diagram offers little predictive ability other than requiring an orbit longer than a hundred days.

The X-ray luminosity measures the mass accretion ( $\dot{M}$ ) onto the NS. Correcting to the 3295 pc distance,  $\dot{M} \approx 1 \times 10^{16}$  g s $^{-1}$ , i.e.  $2 \times 10^{-10} M_{\odot}$  yr $^{-1}$  (Enoto et al. 2014). Such a result may be used to constrain the orbital separation or, equivalently, the orbital period. Indeed, assuming a mass-loss rate for 4U 1954+31 of  $\sim 6 \times 10^{-7} M_{\odot}$  yr $^{-1}$  (Beasor et al. 2020), a terminal wind velocity of 10 – 30 km s $^{-1}$  (Table 4 of Jura & Kleinmann 1990), an orbital eccentricity 0.5, and an orbital separation  $> 5$  AU, a rough estimation of the expected NS wind-accretion rate is  $M_{acc} < 3 \times 10^{-9} M_{\odot}$  yr $^{-1}$  (Bondi & Hoyle 1944). In this context, the mass accretion rate onto the NS estimated from the observed X-ray luminosity implies separation substantially larger than 5 AU. As further evidence favoring this scenario, we note that the optical emission lines are not particularly strong. All together this requires a detached system with an orbital period much longer than 3 yrs.

The semi-major axis of  $\gtrsim 5$  AU is the largest separation of any system classified as symbiotic. However, all other symbiotic systems involve low mass red giants and AGB stars. For instance, the neutron star - M 3 III system V934 Her (Hinkle et al. 2019), has a similarly weak optical emission line spectrum. It has a 12 year orbital period and a semi-major axis of  $\sim 3.7$  AU. The neutron star - M6 III system V2116 Oph (Hinkle et al. 2006), with a rich-emission line spectrum, has a semi-major axis of  $\sim 1.6$  AU. Classification of 4U 1954+31, and other supergiant – degenerate mass transfer systems, in the symbiotic class needs review.

The spin period of 4U 1954+31 is variable with episodes of increasing and decreasing period. Hence, a characteristic age cannot be found (Tauris & Konar 2001). Models by Ho et al. (2020) show that, for long spin periods, the period does not result from prolonged spin-down but is set during the initial  $< 10^6$  years of the NS life. A very long spin period results from a combination of small mass accretion and large NS magnetic field (equation 5 of Ho et al. 2020). The current mass accretion rate

and spin equilibrium period requires an unrealistically strong magnetic field. [Enoto et al. \(2014\)](#) find no evidence for an extreme magnetic field in the 4U 1954+31 NS and suggests a  $\sim 10^{13}$  G field. If the current M I was an unevolved B2 V star at the time of the SN, Reimer’s law scales the mass loss down by a factor of  $10^3$ . If the accretion similarly was  $10^3$  less, the magnetic field of the newly born NS was  $10^{15}$  G. This suggests that the current M I was a MS star at the time of the SN. Since most of the stellar life is spent in the core hydrogen burning stage, this seems a reasonable conclusion.

#### 4.4. OB Association Membership

High energy X-ray sources are often associated with star forming regions in the galactic arms ([Chaty 2011](#)). 4U 1954+31 is located in Vulpecula,  $3.7^\circ$  from the Vul OB2 association ([Ruprecht et al. 1982](#)). This is a complex star forming region marking the Orion-Cygnus arm. Gaia distances,  $3295_{-62}^{+985}$  pc for 4U 1954+31 and  $\sim 4.4$  kpc for Vul OB2, place 4U 1954+31 in the foreground of Vul OB2. The proper motions of 4U 1954+31 and Vul OB2 are similar, but not identical differing by  $\sim 1.4$  milliarcsecond in RA, i.e.  $21 \text{ km s}^{-1}$  at 3.2 kpc. We conclude that 4U 1954+31 is likely not a member of Vul OB2. On the other hand, the A and B supergiants in Vul OB2 ([Turner 1980](#)) exhibit a range of distance, proper motion, and velocity. The family of space motions is similar to the space motion of 4U 1954+31. [Drazinos et al. \(2013\)](#) found that OB associations in spiral galaxies have average diameters of  $\sim 500$  pc with star forming regions several times this size. Association membership in this region is a complex problem and beyond the scope of this paper. The general agreement of proper motions and velocities of the stars in this field, including 4U 1954+31, does demonstrate that the 4U 1954+31 NS did not receive a large kick velocity from the SN.

## 5. DISCUSSION

### 5.1. Implications for the X-ray source

The discovery that 4U 1954+31 is a late-type supergiant – NS binary impacts four parameters of interest in understanding the X-ray properties. First, the distance is  $\gtrsim 1.9$  times larger than would be derived from the luminosity of the late-type star by assuming it is a giant. Hence, the luminosity of the X-ray source is  $\sim 4$  times larger. Second, the system is young and the NS has evolved to its current state in a few tens of megayears. Third, the separation of the NS and M giant is greater than previously seemed likely. Fourth, the mass loss rate from the late-type star is larger than previously believed. Re-scaling the accretion rate onto the NS with the mass of the late-type star is a complex problem because a change of the M star mass also affects the orbital parameters and, in turn, the accretion rate.

The M supergiant mass-loss rate prescription of [Beasor et al. \(2020\)](#) and the range of luminosity and mass in Table 2 yield a broad possible range of mass-loss rates,  $\dot{M}$ , from  $10^{-5}$  to  $10^{-8} M_\odot \text{ yr}^{-1}$ . For the preferred values of  $9 M_\odot$  and  $43880 L_\odot$ ,  $\dot{M} \sim 6 \times 10^{-7} M_\odot \text{ yr}^{-1}$ . A M4 giant has a decidedly lower  $\dot{M}$ ,  $\lesssim 10^{-8}$  ([Olofsson et al. 2002](#); [Groenewegen et al. 2014](#)). The mass loss process for M giants and supergiants results from radiation pressure on dust. The circumstellar flow is cold,  $T < 300$  K, with the terminal wind velocity,  $v_\infty$ , in the range 10 to 30  $\text{km s}^{-1}$  ([Jura & Kleinmann 1990](#)). Studies of the bright M I  $\alpha$  Ori are a source of detailed information. This star has a terminal circumstellar expansion velocity of  $14.3 \text{ km s}^{-1}$  ([Huggins 1987](#)). An extensive summary of observational parameters and references to the literature for  $\alpha$  Ori can be found in [Dolan et al. \(2016\)](#). For  $\alpha$  Ori  $\dot{M} = 2 \pm 1 \times 10^{-6} M_\odot \text{ yr}^{-1}$ . By way of comparison, typical temperatures and terminal wind velocities for the outflow in early-type HMXB are 30000 K and  $1000 \text{ km s}^{-1}$ . Modified wind momentum  $\log(\dot{M} v_\infty R_*^{1/2})$ , is

commonly used to describe hot star winds. Ignoring the very different mass loss physics between hot and cold winds, the modified wind momentum for  $\alpha$  Ori is  $27.7 \text{ (g cm s}^{-2} \text{ R}_{\odot}^{1/2})$ . The modified wind momentum of the M supergiants falls on the lower end of the wind-momentum luminosity relation for massive stars (see Figure 5 of Hainich et al. 2020).

In the case of wind accretion, the accretion rate onto the NS scales linearly with the mass donor mass-loss rate, but decreases as  $v_{wind}^{-3}$  (Boffin & Jorissen 1988) where  $v_{wind}=v_{\infty}+v_{orb}$ . More intense mass loss results in more accretion, but a faster wind reduces the maximum radius below which the wind is trapped into the gravitational potential well of the NS. For the long orbital period system 4U 1954+31,  $v_{orb}$  is a few  $\text{km s}^{-1}$ , a fraction of the terminal wind velocity. As a first approximation this modulating term to the NS accretion can be ignored. The X-ray luminosity of 4U 1954+31 implies a mass accretion rate of  $2 \times 10^{-10} \text{ M}_{\odot} \text{ yr}^{-1}$  (Enoto et al. 2014, adjusted to 3.3 kpc distance), implying that only a few parts per thousand of the mass loss from the supergiant are captured by the NS. This can be compared to the M 3 III – NS system V934 Her. The wind velocity is likely similar but the mass loss rate is at least an order of magnitude less. The mass accretion rate for the V934 Her NS is  $\sim 10^{-14} \text{ M}_{\odot} \text{ yr}^{-1}$  (Masetti et al. 2002). This scales from that of 4U 1954+31 with the difference in mass loss rates in agreement with the wind accretion relations of Boffin & Jorissen (1988).

### 5.2. Evolution Scenario

The standard scenario for the evolution of HMXB (Canal et al. 1990; Tauris & van den Heuvel 2006; Tauris et al. 2017) invokes the evolution of two stars with zero-age MS masses sufficient for the stars to terminate in a core-collapse SN. The binary system must have a sufficiently short period so that the stars will interact as they evolve. Evolution of the more massive star results in large scale mass transfer through Roche lobe overflow. Extreme mass loss from this star produces a roughly  $3.5 \text{ M}_{\odot}$  helium star, i.e. the stripped core of the massive star. The helium star undergoes a low luminosity core collapse SN resulting in a system with a NS and a massive star. Mass accretion onto the secondary widens the orbit resulting in an eccentric orbit of period around 15 years. The system now appears as a HMXB as mass loss from the former secondary, now the high mass primary, is accreted onto the NS. As the massive star evolves mass loss decreases the orbital period. The terminal stage of the HMXB is a common envelope (CE) phase that ejects mass from the system producing a helium star. Following the core collapse SN of the helium star a NS - NS binary results with an orbital period of hours. A system of this type radiates gravity wave radiation and, if the orbit is short enough, will merge.

The 4U 1954+31 system originated with two high-mass stars. The lack of a kick velocity for 4U 1954+31 supports an origin of the NS from an ultra-stripped progenitor, either through an electron capture instability SN (Kochanek et al. 2019) or low-mass iron core-collapse SN (Tauris et al. 2017). In addition, the current orbit is both eccentric and has a period of multiple years.

### 5.3. Mass limits and the super-AGB

The FuNS models shown in Figure 3 follow the evolutionary path up to the final stages of burning. On the base of the observed location in the HR diagram, a range of mass, perhaps as low as  $7 \text{ M}_{\odot}$  and as high as  $15 \text{ M}_{\odot}$ , must be considered for the M star in 4U 1954+31. Models with  $M \geq 10 \text{ M}_{\odot}$  attain the brightest point of the corresponding track during the C burning and, later on, their luminosity does not change for a few thousand years until the final collapse. The two magenta lines

in Figure 3 are for the two smaller masses, namely 7 and 9  $M_{\odot}$ . The smaller mass coincides with the minimum mass of a star that can attain the conditions for the C ignition. Less massive stars skip the C burning, enter the AGB and terminate their life as CO white dwarfs. The 7  $M_{\odot}$  star, ignites C off centre in degenerate conditions and, after an incomplete C burning, enters the super-AGB phase. Thus, the brightest point of the track corresponds to the luminosity at the beginning of the super-AGB. This star will end as a C-O-Ne WD of mass of about 1.1  $M_{\odot}$ .

The 9  $M_{\odot}$  model, on the contrary, experiences an almost complete C-burning phase that leaves a degenerate O-Ne-Mg core. Then, this star also moves to the super-AGB phase. The brightest point of the track is attained after the first few thermal pulses. The C ignition occurs at  $\log(L/L_{\odot}) \approx 4.5$ , but in the following evolution, the luminosity increases up to  $\log(L/L_{\odot}) \sim 5.1$ . This transition at high luminosity is quite fast. During the super-AGB the luminosity may further increase because of the occurrence of the hot bottom burning (Doherty et al. 2014). The duration of this phase, depending on the mass loss rate, could be a few times  $10^4$  years (9  $M_{\odot}$ ), up to  $10^5$  years (7  $M_{\odot}$ , see Doherty et al. 2015). Since in the 9  $M_{\odot}$  model the degenerate core is about 1.3  $M_{\odot}$ , very close to the Chandrasekhar limit, it is possible that the core will undergo an electron capture instability, giving rise to either a core-collapse or a thermonuclear explosion (e-capture SN, Woosley & Heger 2015).

The best match of the observed HRD location is obtained for an initial mass between 7 and 11  $M_{\odot}$ . In general, we have to consider the time spent by the star in each portion of the track. In this context, a more massive object cannot be excluded, even if its effective temperature appears higher than observed. Indeed, the effective temperature of a model may be affected by radiative opacity uncertainties (atomic and molecular opacity, in particular). In addition, it also depends on the adopted mixing length parameter that, as usual, has been calibrated using the Sun. It is not clear whether this calibration is appropriate for a red supergiant. A further phenomenon that may affect the quoted mass range is rotation. Indeed, a fast rotation during the main sequence phase implies larger final core masses, and, in turn, higher luminosities during the post-MS evolution. Unfortunately, the MS rotation velocity of the M star in 4U 1954+31 is indeterminate. In spite of these uncertainties, we feel confident excluding an initial mass  $< 7 M_{\odot}$ .

#### 5.4. Comparison with Abundances

The surface abundances of the red supergiant in the 4U 1954+31 system are the result of the original composition, stellar evolution and mixing processes and, possibly, mass transfer from the proto-NS primary as it evolved. Single star models of 9-15  $M_{\odot}$ , starting from solar abundance ratios, indicate that [C/Fe], [N/Fe], and [O/Fe] after the first dredge up (FDU) should be  $-0.25$ ,  $+0.55$ , and  $-0.07$ , respectively. The  $^{12}\text{C}/^{13}\text{C}$  ratio is predicted to be  $\sim 20$ .  $^{16}\text{O}/^{17}\text{O}$  and  $^{16}\text{O}/^{18}\text{O}$  are both around 750 in the 13  $M_{\odot}$  model and 650-700 in the 9  $M_{\odot}$  model. In a 10.8  $M_{\odot}$  model by Takahashi et al. (2013), the post-FDU composition is  $^{12}\text{C}/^{13}\text{C}=20$ ,  $^{16}\text{O}/^{17}\text{O}=810$ , and  $^{16}\text{O}/^{18}\text{O}=660$ . Takahashi et al. report of a dredge-out episode occurring at the end of the C-burning phase, causing a sharp increase of the  $^{18}\text{O}$  abundance at the stellar surface and, in turn, a substantial drop of  $^{16}\text{O}/^{18}\text{O}$  to about 40. In the case of a super-AGB star, the HBB should also produce sizeable modifications of the post-FDU composition. A significant increase in the N abundance is expected, while  $^{12}\text{C}$  should be reduced (Doherty et al. 2014). Isotopic ratios of C and O are predicted to change as well:  $^{12}\text{C}/^{13}\text{C}$  and  $^{16}\text{O}/^{17}\text{O}$  are both expected to go down, while  $^{16}\text{O}/^{18}\text{O}$  should increase. Then, the possible coupling of HBB and third dredge up may cause an increase of the C+N+O.

Comparison of these predictions with the derived 4U 1954+31 abundances should constrain its evolutionary status. The predicted post-FDU nitrogen is in good agreement with the observed value, while the predicted C and O depletion are slightly smaller than observed, but within the uncertainty. In addition, the CNO abundances sum up, within the uncertainties, to the solar CNO value scaled to the observed metallicity, in accordance with measurements from other M supergiants (Lyubimkov et al. 2019). In contrast, no clear evidence of HBB or third dredge-up is found. This, however, does not exclude that the M supergiant in 4U 1954+31 could be a star with mass in the range 7-10  $M_{\odot}$ , provided that its present evolutionary status is beyond the C ignition and before the occurrence of the first thermal pulses during the super-AGB phase.

At variance with the elemental CNO abundances, the post-FDU isotopic composition does not comply with the observed values. The measured  $^{12}\text{C}/^{13}\text{C}$ ,  $9\pm 2$ , is clearly less than the predicted value. Harris & Lambert (1984) found similar  $^{12}\text{C}/^{13}\text{C}$  for the supergiants  $\alpha$  Ori and  $\alpha$  Sco. The oxygen isotopic ratios come with considerable observational uncertainties, in particular for  $^{16}\text{O}/^{18}\text{O}$  where the measured value relies on a single line. Both the observed  $^{16}\text{O}/^{17}\text{O}$  and  $^{16}\text{O}/^{18}\text{O}$  ratios appear higher than the values expected after the FDU. In the case of a super-AGB star undergoing HBB, the match with the observed  $^{16}\text{O}/^{18}\text{O}$  would be better but the difference with the observed  $^{16}\text{O}/^{17}\text{O}$  would be even worse. Note, however, that our isotopic predictions start from solar abundance ratios and that a deviation from this hypothesis is not unusual in young star forming regions influenced by supernova explosions. In any case, due to the large uncertainties, we cannot put much weight on the comparison of observed and modeled oxygen isotopic ratios.

Mass transfer from the more evolved star may be a significant factor in altering the abundance pattern of a star belonging to a close binary system. The lack of kick velocity for the NS in 4U 1954+31 suggests that the MS primary became a He star before core collapse. The mass of this star at the time of core collapse was likely in the 3 - 4  $M_{\odot}$  range (Tauris et al. 2017). Since this star had a main sequence mass  $\gtrsim 9 M_{\odot}$  it lost  $\gtrsim 5 M_{\odot}$ . The mass loss process was most likely Roche lobe overflow onto the secondary (Tauris et al. 2017). The evolution of a system of this type is complex and depends on the orbit. The Roche lobe mass transfer will spin up the accretor, stopping mass accretion (de Mink et al. 2013). For a Roche lobe filling supergiant a common envelope develops, since as the supergiant loses mass it continues to expand. The expectation is that the envelope of the donor is ejected and the secondary star left relatively unaffected (de Mink et al. 2013).

In addition to this mass transfer event, the present-day supergiant then was exposed to the SN ejecta. Either accretion of the material ejected by the SN or ablation of the stellar envelope are possible. Based on the measured abundances, the only indication of a possible SN pollution are the over-abundances of the r-process element Sc and the iron peak element Mn. However, the Sc abundance is suspect. Thorsbro et al. (2018) found that for the near-infrared Sc lines non-LTE effects result in the abundance being overestimated at  $T_{eff} < 3800$  K. Pollution may differ from one element to another, depending on the initial abundance. In addition, a large overabundance of  $\alpha$ -elements, such as O or Ti, are expected in case of a SN pollution, in contrast with the observed abundance pattern. Alternatively, it is also possible that the fast wind from the SN had stripped part of the envelope, leaving no trace of either the SN or of mass transferred before the SN.

### 5.5. Ages and Life Expectancy

The creation of the NS erases most information about the progenitor. Certainly the progenitor was massive enough to undergo a core collapse, but not too massive, otherwise the compact remnant

would be a BH instead of a NS. Hills (1983) discusses the effects of the sudden mass loss, i.e. a SN, on the orbit. The survival of the binary, in the event that the SN was from a massive star core collapse, potentially provides limits on the mass. However, the lack of a kick velocity requires that the SN resulted from an ultra-stripped star. The progenitor of the NS, since it evolved faster, was initially the more massive star in the binary. Since the M I possibly could evolve into a massive WD, the mass limits of the MS primary are just those of a star producing a NS,  $9 M_{\odot} \lesssim M \lesssim 25 M_{\odot}$ . The upper mass bound actually depends on the upper mass limit for a NS, the so-called Tolman-Oppenheimer-Volkoff mass, a quantity affected by large uncertainties. In addition, in the case of a rather small progenitor, the collapse may form a BH rather than a NS, directly or by fall back, depending on the compactness of the pre-supernova structure (O’Connor & Ott 2011). The lifetime of a  $25 M_{\odot}$  is 7 Myr and of a  $9 M_{\odot}$  30 Myr. The M I star has a mass  $7 M_{\odot} \lesssim M \lesssim 15 M_{\odot}$ . Since this star has exhausted core hydrogen it is effectively at the end of its life and its age is 50 Myr ( $7 M_{\odot}$ ) to 12 Myr ( $15 M_{\odot}$ ). The lack of a SN remnant constrains the time that has elapsed since the SN to  $\gtrsim 10^5$  years (Stafford et al. 2019), giving the minimum age of the NS. The difference in stellar lifetimes sets the maximum age of the NS at 43 Myr.

There are  $\sim 114$  HMXB known (Chaty 2018). These systems all contain hot stars with 4U 1954+31 the only late-type system. This likely reflects the lifetime as a red rather than blue supergiant. In the mass range  $10 - 20 M_{\odot}$ , the “normal” stellar wind is not enough to completely erode the H-rich envelope and the star remains in the red supergiant branch up to the core collapse. In the case of enhanced mass loss, for instance in close binaries, the star can return to the blue before the final collapse. In the mass range  $7 - 10 M_{\odot}$ , the situation can be more complicated for the stars that enter a super-AGB phase after C burning. During the super-AGB, the core mass increases, while the envelope is progressively lost. If the core mass attains the Chandrasekhar limit before the envelope is reduced down to a few tenths of a solar mass, a SN occurs when the star is a red supergiant. If not, i.e., if the H-rich envelope is almost completely eroded, the star moves to the blue, ending as a (C-)O-Ne-Mg WD.

## 6. CONCLUSIONS

4U 1954+31 is shown to be a M supergiant – NS binary. The M companion to the NS had previously been identified as a M III (Masetti et al. 2006). Gaia data show that the luminosity of the M star is too high for the star to be a normal giant. The near-IR spectrum is a good match to spectral type M4 I. From the excitation temperature of the  $1.6 \mu\text{m}$  CO,  $T_{\text{eff}} = 3450^{+100}_{-50}$  K, in agreement with the spectral type. Optical through mid-IR photometry combined with the Gaia parallax give a luminosity  $= 43880^{+34070}_{-15900} L_{\odot}$  and radius  $= 586^{+188}_{-127} R_{\odot}$ . Spectrum synthesis suggests a surface gravity ( $\log g$ ) of  $-0.15 \pm 0.25$  ( $\text{cm s}^{-1}$ ) corresponding to a  $9 - 12 M_{\odot}$  star. Evolutionary tracks indicate that the mass is  $9^{+6}_{-2} M_{\odot}$ . A time series of velocities from high resolution optical spectra tracks part of the orbit. The orbital period is  $\gtrsim 3$  yrs, in agreement with the limit set from the Roche lobe of a  $9 M_{\odot}$  supergiant plus a  $1.4 M_{\odot}$  NS binary.

Although the existence of a binary system containing a M supergiant plus NS is expected from stellar evolution theory, this is the first such system to be identified. The binary shares characteristics of both high and low mass X-ray binaries. It also has been grouped with the symbiotic X-ray binaries. However, no other symbiotic binary contains a supergiant and the standard model of the symbiotic class excludes it (Kenyon & Webbink 1984). Considered as a symbiotic system, it has the largest known semi-major axis,  $> 4.5$  AU.

The lack of a kick velocity argues for the origin of the NS in a low luminosity core collapse SN. This requires that the mass of the primary to be reduced by at least  $5 M_{\odot}$  before core collapse, likely by a CE event. The current M supergiant was a B MS star when the originally more massive star went SN. The abundances for the M I are not exceptional. No trace of the CE or SN events appears in the abundances. This is either the result of the SN ablating the surface of the B MS star or subsequent mixing of the surface material into the envelope as the B star evolved. Roche lobe mass transfer onto the MS B star could have spun up the star, enhancing meridional mixing. Using the lowest possible mass of the M supergiant to constrain the age of the 4U 1954+31 NS, the NS age is  $\lesssim 43$  Myr.

#### ACKNOWLEDGMENTS

The authors thank Bernhard Aringer for giving access to his spectral synthesis code and for support with the computations. NOAO reference librarian Sharon Hunt helped us access obscure reference materials. SM plot, developed by Robert Lupton and Patricia Monger, was used in the production of some figures. This research was facilitated by the SIMBAD database, operated by CDS in Strasbourg, France, the VizieR catalogue access tool, CDS, Strasbourg, France (DOI: 10.26093/cds/vizie), and the Astrophysics Data System Abstract Service, operated by the Smithsonian Astrophysical Observatory under NASA Cooperative Agreement NNX16AC86A. This work made use of data from the European Space Agency (ESA) mission *Gaia* (<https://www.cosmos.esa.int/gaia>), processed by the Gaia Data Processing and Analysis Consortium (DPAC). Funding for the DPAC has been provided by national institutions, in particular the institutions participating in the *Gaia* Multilateral Agreement. This work used IGRINS, developed under a collaboration between the University of Texas at Austin and the Korea Astronomy and Space Science Institute (KASI) with the financial support of the US National Science Foundation under grants AST-1229522 and AST-1702267, of the University of Texas at Austin, and of the Korean GMT Project of KASI. This publication makes use of data obtained with the Lowell Discovery Telescope (LDT) at Lowell Observatory. Lowell is a private, non-profit institution dedicated to astrophysical research and public appreciation of astronomy and operates the LDT in partnership with Boston University, the University of Maryland, the University of Toledo, Northern Arizona University and Yale University. NSF's National Optical-Infrared Astronomy Research Laboratory (NOIRLab), which supersedes the National Optical Astronomy Observatory (NOAO), is operated by the Association of Universities for Research in Astronomy under a cooperative agreement with the National Science Foundation. IRAF (Image Reduction and Analysis Facility) software was distributed by NOAO. KH and RJ express their thanks to the NOAO Office of Science and the NOIRLab RSS group for support of this research. The research at Tennessee State University was supported in part by the State of Tennessee through its Centers of Excellence program.

OCHID identification numbers: KENNETH H. HINKLE [0000-0002-2726-4247], THOMAS LEBZELTER [0000-0002-0702-7551], FRANCIS C. FEKEL [0000-0002-9413-3896], OSCAR STRANIERO [0000-0002-5514-6125], RICHARD R. JOYCE [0000-0003-0201-5241], LISA PRATO [0000-0001-7998-226X], NICOLE KARNATH [0000-0003-3682-854X], NOLAN HABEL [0000-0002-2667-1676]

## REFERENCES

- Aringer, B., Girardi, L., Nowotny, W., et al. 2016, *MNRAS*, 457, 3611
- Bailer-Jones, C.A.L., Rybizki, J., Foesneau, M. et al. 2018, *AJ*, 156, 58
- Baumgartner, W.H., Tueller, J., Markwardt, C.B., et al. 2013, *ApJS*, 207, 19
- Beasor, E.R., Davies, B., Smith, N., et al. 2020, *MNRAS*, 492, 5994
- Bird, A.J., Bazzano, A., Malizia, A., et al. 2016, *ApJS*, 223, 15
- Boffin, H.M.J. & Jorissen, A. 1988, *A&A*, 205, 155
- Bondi, H., & Hoyle, F. 1944, *MNRAS*, 104, 273
- Bodaghee, A., Courvoisier, T.J.-L., Rodriguez, J., et al. 2007, */aap*, 467, 585
- Brooke, J. S. A., Ram, R. S., Western, C. M., et al. 2014, *ApJS*, 210, 23
- Canal, R., Isern, J., & Labay, J. 1990, *Ann. Rev. Astro. Astrophys.*, 28, 183
- Carr, J. S., Sellgren, K., & Balachandran, S. C. 2000, *ApJ*, 530, 307
- Chaty, S. 2011 in “Evolution of compact binaries” ASP Conf. Series, 447, L. Schmidtbreich, M. Schreiber, & C. Tappert eds., p 29
- Chaty, S. 2018, in Proceedings of Fourteenth Marcel Grossmann Meeting On Recent Developments in Theoretical and Experimental General Relativity, Astrophysics, and Relativistic Field Theories. Eds. Massimo Bianchi, Robert T Jansen & Remo Ruffini (Singapore, World Scientific Publishing Co.), pp. 1883-1888
- Corbet, R., Barbier, L., Barthelmy, S. et al. 2006, *ATel*, 797
- Corbet, R.H.D., Sokoloski, J.L., Mukai, K. et al. 2008, *ApJ*, 675, 1424
- de Mink, S.E., Langer, N., Izzard, R.G., et al. 2013, *ApJ*, 764, 166
- Doherty, C. L., Gil-Pons, P., Lau, H. H. B., et al. 2014, *MNRAS*, 437, 195
- Doherty, C. L., Gil-Pons, P., Siess, L., et al. 2015, *MNRAS*, 446, 2599
- Dolan, M.M., Mathews, G.J., Lam, D.D. et al. 2016, *ApJ*, 819, 7
- Drazinos, P., Kontizas, E., Karampelas, A., et al. 2013, *A&A*, 553, 87
- Eaton, J. A., & Williamson, M. H. 2007, *PASP*, 119, 886
- Eggleton, P. P. 1983, *ApJ*, 268, 368
- Enoto, T., Sasano, M., Yamada, S., et al. 2014, *ApJ*, 786, 127
- Escorza1, A., Siess, L., Van Winckell, H., et al. 2020, *A&A*, in press.
- Fekel, F. C., Tomkin, J., & Williamson, M. H. 2009, *AJ*, 137, 3900
- Fekel, F. C., Rajabi, S., Muterspaugh, M. W., Williamson, M. W. 2013, *AJ*, 145, 111
- Forman, W. Jones, C., Cominsky, L., et al. 1978, *ApJS*, 38, 357
- Gaia* Collaboration; Brown, A. G. A., Vallenari, A., Prusti, T., et al. 2018, *A&A*, 616, 10
- Groenwegen, M.A.T. 2014, *A&A*, 561, L11
- Hainich, R., Oskinova, L.M., Torrejón, J.M., et al. 2020, *A&A*, 634, A49
- Harris, M.J. & Lambert, D.L. 1984, *ApJ*, 281, 739
- Hills, J.G. 1983, *ApJ*, 267, 322
- Hinkle, K., Wallace, L., & Livingston, W.C. 1995, “Infrared Atlas of the Arcturus Spectrum, 0.9 – 5.3  $\mu\text{m}$ ”, (San Francisco:ASP)
- Hinkle, K.H., Fekel, F.C, Joyce, R.R., et al. 2006, *ApJ*, 641, 479
- Hinkle, K.H., Lebzelter, T., & Straniero, O. 2016, *ApJ*, 825 (HLS16)
- Hinkle, K.H., Fekel, F.C., Joyce, R.R., et al. 2019, *ApJ*, 872, 43
- Ho, W.C.G., Wijngaarden, J.P., Andersson, N., et al. 2020, *MNRAS*, 494, 44
- Huggins, P.J. 1987, *ApJ*, 313, 400
- Jura, M., & Kleinmann, S. G. 1990, *ApJS*, 73, 769
- Kaplan, D.L., Levine, A.M., Chakrabarty, D. et al. 2007, *ApJ*, 661, 437
- Kenyon, S.J. & Webbink, R.F. 1984, *ApJ*, 279, 252
- Knigge, C., Coe, M.J., Podsiadlowski, P. 2011, *Nature*, 479, 372
- Kochanek, C.S., Auchettl, K., & Belczynski, K. 2019, *MNRAS*, 485, 5394
- Krivonos, R., Tsygankov, S., Revnivtsev, M., et al. 2010, *A&A*, 523, A61
- Lambert, D. L., Brown, J. A., Hinkle, K. H., et al. 1984, *ApJ*, 284, 223
- Lebzelter, T., Hinkle, K. H., Straniero, O., et al. 2019, *ApJ*, 886, 117
- Levesque, E.M., Massey, P., Olsen, K.A.G., et al. 2005, *ApJ*, 628, 973
- Li, G., Gordon, I. E., Rothman, L. S., et al. 2015, *ApJS*, 216, 15

- Liu, Q.Z., van Paradijs, J., & van den Heuvel, E.P.J. 2007, *A&A*, 469, 807
- Lü, G.-L., Zhu, C.-H., Postnov, K.A. et al. 2012, *MNRAS*, 424, 2265
- Lyubimkov, L.S., Korotin, S.A., & Lambert, D.L. 2019, *MNRAS*, 489, 1533
- Marcu, D.M., Fürst, F., Pottschmidt, K. et al. 2011, *ApJL*, 742, L11
- Masetti, N., Dal Fiume, D., Cusumano, G. et al. 2002, *A&A*, 382, 104
- Masetti, N., Orlandini, M., Palazzi, E. et al. 2006, *A&A*, 453, 295
- Masetti, N., Rigon, E., Maiorano, E. et al. 2007, *A&A*, 464, 277
- Mattana, F., Götz, D., Falanga, M. et al. 2006, *A&A*, 460, L1
- Merrill, P.W. 1958, *Mem. Soc. R. Sci. Liège, Ser. 4*, 20, 436
- Mürset, U., Wolff, B., & Jordan, S. 1997, *A&A*, 319, 201
- Nebot Gómez-Morán, A., Motch, C., Pineau, F.-X., et al. 2015, *MNRAS*, 452, 884
- O'Connor, E., & Ott, C. D. 2011, *ApJ*, 730, 70
- Olofsson, H., González, D.D., Kerschbaum, F. et al. 2002, *A&A*, 391, 1053
- Park, C., Jaffe, D.T., Yuk, I.-S., et al. 2014, *Proc. SPIE*, 9147, 1DV
- Pilachowski, C., Hinkle, K.H., Young, M.D. et al. 2017, *PASP*, 129, 024006
- Ruprecht, J., Balazs, B., White, R.E. 1982, *Bulletin d'Information du Centre de Données Stellaires*, No. 22, 132
- Sander, A.A.C. 2018, in "High-mass X-ray binaries", *Proc. IAU Symp.* 346, eds. L.M. Oskinova et al. , p.17
- Scarfe, C.,D., Batten, A. H., & Fletcher, J. M., 1990, *Publ. of Dominion Astrophys. Obs. Victoria*, 18, 21
- Schlafly, E.F. & Finkbeiner, D.P. 2011, *ApJ*, 737, 103  
(<https://irsa.ipac.caltech.edu/applications/DUST/>)
- Smith, V. V., Cunha, K., Shetrone, M. D., et al. 2013, *ApJ*, 765, 16
- Stafford, J.N., Lopez, L.A., Auchetti, K., et al. 2019, *ApJ*, 884, 113
- Straniero, O., Gallino, R., & Cristallo, S. 2006, *NuPhA*, 777, 311
- Straniero, O., Dominguez, I., Piersanti, L., et al. 2019 *ApJ*, 881, 158
- Takahashi, K., Yoshida, T., Umeda, H. 2013, *ApJ*, 771, 28
- Tauris, T.M. & Konar, S. 2001, *A&A*, 376, 543
- Tauris, T.M. & van den Heuvel, E.P.J. 2006 in "Compact Stellar X-ray Sources," eds W. Lewin & M. van der Klis, *Cambridge Astrophysics Series 39*, (Cambridge, UK: Cambridge University Press), p. 623
- Tauris, T. M., Kramer, M., Freire, P.C.C., et al. 2017, *ApJ*, 846, 170
- Thorsbro, B., Ryde, N., Schultheis, M., et al. 2018, *ApJ*, 866, 52
- Turner, D.G. 1980, *ApJ*, 235, 146
- Tweedy, R.W., Warwick, R.S. & Remillard, R. 1989, in "Two Topics in X-Ray Astronomy, Vol. 1: X-Ray Binaries," ed. J. Hunt & B. Battrick, p. 661.
- Wallace, L. & Hinkle, K.H. 1997, *ApJS*, 111, 445
- Woosley, S. E., & Heger, A. 2015, *ApJ*, 810, 34
- Yungelson, L.R., Kuranov, A.G., & Postnov, K.A. 2019, *MNRAS*, 485, 851

**Table 1.** Table of Observations and Velocities

| HJD<br>-2450000 | RV <sup>a</sup><br>(km s <sup>-1</sup> ) | Observatory/<br>Spectrograph |
|-----------------|--|------------------------------|
| 8039.711        | -1.4                                     | AST/FFES                     |
| 8041.772        | -1.2                                     | AST/FFES                     |
| 8042.632        | -1.4                                     | AST/FFES                     |
| 8043.624        | -1.4                                     | AST/FFES                     |
| 8226.859        | 0.1                                      | AST/FFES                     |
| 8417.708        | 3.3                                      | AST/FFES                     |
| 8423.686        | 3.5                                      | AST/FFES                     |
| 8439.661        | 4.1                                      | AST/FFES                     |
| 8445.616        | 4.0                                      | LDT/IGRINS                   |
| 8456.601        | 5.1                                      | AST/FFES                     |
| 8465.621        | 5.4                                      | AST/FFES                     |
| 8532.005        | 6.1                                      | AST/FFES                     |
| 8540.965        | 6.0                                      | AST/FFES                     |
| 8565.999        | 6.1                                      | AST/FFES                     |
| 8599.945        | 5.8                                      | AST/FFES                     |
| 8627.932        | 6.3                                      | AST/FFES                     |
| 8661.804        | 6.0                                      | AST/FFES                     |
| 8739.754        | 6.4                                      | AST/FFES                     |
| 8767.642        | 5.9                                      | AST/FFES                     |
| 8768.642        | 6.2                                      | AST/FFES                     |
| 8800.620        | 6.4                                      | AST/FFES                     |
| 8801.620        | 6.4                                      | AST/FFES                     |
| 8963.837        | 5.3                                      | AST/FFES                     |
| 8964.920        | 5.8                                      | AST/FFES                     |
| 8965.921        | 5.7                                      | AST/FFES                     |
| 9020.692        | 6.1                                      | AST/FFES                     |
| 9024.794        | 6.1                                      | AST/FFES                     |
| 9025.794        | 6.0                                      | AST/FFES                     |

<sup>a</sup>Heliocentric. To correct to LSR add  
17.77 km s<sup>-1</sup>

**Table 2.** Parameters of the 4U 1954+31 M supergiant

| Parameter               | Value                                   | Source                                 |
|-------------------------|---|--|
| Distance                | $3295^{+985}_{-631}$ pc                 | <i>Gaia</i> Bailer-Jones et al. (2018) |
| Spec Type               | M4 I                                    | Fig. 1; $T_{eff}$ & luminosity         |
| $T_{eff}$               | $3450^{+100}_{-50}$ K                   | Sp.Ty.; CO $T_{exc}$                   |
| Luminosity              | $43880^{+34070}_{-15900}$ $L_{\odot}$   | Photometry, see text; Fig. 2           |
| Radius                  | $586^{+188}_{-127}$ $R_{\odot}$         | Fig. 2                                 |
| Mass                    | $9^{+6}_{-2}$ $M_{\odot}$               | Luminosity & Evol. tracks              |
| Surface gravity (log g) | $-0.15 \pm 0.25$ ( $\text{cm s}^{-1}$ ) | Mass & radius                          |
| $[Fe/H]$                | $-0.4 \pm 0.2$                          | See text                               |
| Age                     | $\sim 12 - 50$ Myr                      | Evol. tracks                           |

**Table 3.** Atomic Line List

| Element | wavenumber<br>( $\text{cm}^{-1}$ ) | Element | wavenumber<br>( $\text{cm}^{-1}$ ) |
|---------|------------------------------------|---------|------------------------------------|
| Na I    | 4527.0                             | Fe I    | 4732.7                             |
|         | 4532.6                             |         | 5786.3                             |
| Al I    | 4739.6                             |         | 5786.3                             |
|         | 5963.8                             |         | 5810.9                             |
|         | 5968.3                             |         | 5812.3                             |
|         | 5979.6                             |         | 5814.8                             |
| Si I    | 5593.3                             |         | 5825.5                             |
|         | 5940.8                             |         | 5867.7                             |
|         | 6165.2                             |         | 5876.9                             |
|         | 6185.0                             | V I     | 4582.4                             |
|         | 6211.5                             |         | 4786.5                             |
|         | 6224.9                             |         | 6033.2                             |
|         | 6313.9                             |         | 6277.8                             |
| Sc I    | 4489.8                             | Mn I    | 6569.5                             |
|         | 4501.8                             | Ti I    | 4419.4                             |
|         | 4530.8                             |         | 4454.3                             |
|         | 4533.5                             |         | 4481.0                             |
|         | 4583.3                             |         | 4488.3                             |
|         | 4600.6                             |         | 4496.6                             |
| Fe I    | 4382.3                             |         | 4501.0                             |
|         | 4419.7                             |         | 4543.3                             |
|         | 4444.4                             |         | 4565.5                             |
|         | 4458.0                             |         | 4589.5                             |
|         | 4468.0                             |         | 4691.7                             |
|         | 4507.7                             |         | 4793.6                             |
|         | 4654.2                             |         | 5874.5                             |
|         | 4707.1                             |         | 5883.3                             |
|         | 4712.1                             |         | 6431.7                             |
|         | 4720.6                             |         |                                    |

**Table 4.** Molecular Line List

| Molecule         | transition | wavenumber<br>( $\text{cm}^{-1}$ ) |
|------------------|------------|------------------------------------|
| $^{12}\text{CO}$ | 9-6 head   | 5920–5940                          |
|                  | 8-5 head   | 6005–6020                          |
|                  | 7-4 head   | 6086–6098                          |
|                  | 6-3 head   | 6167–6177                          |
|                  | 5-2 head   | 6245–6257                          |
|                  | 4-2 R18    | 4212.7                             |
|                  | 2-0 P11    | 4213.9                             |
|                  | 2-0 P9     | 4223.0                             |
|                  | 3-1 R4     | 4225.2                             |
|                  | 4-2 R24    | 4225.7                             |
|                  | 4-2 R27    | 4231.2                             |
|                  | 4-2 R28    | 4232.8                             |
|                  | 3-1 R7     | 4235.1                             |
|                  | 4-2 R31    | 4237.4                             |
|                  | 3-1 R8     | 4238.3                             |
|                  | 3-1 R9     | 4241.4                             |
|                  | 4-2 R36    | 4243.6                             |
|                  | 3-1 R84    | 4260.2                             |
|                  | 2-0 R1     | 4267.5                             |
|                  | 6-3 P18    | 6030.1                             |
|                  | 5-2 P30    | 6033.9                             |
|                  | 6-3 P17    | 6035.6                             |
|                  | 4-1 P35    | 6076.4                             |
|                  | 7-4 R46    | 6087.9                             |
|                  | 7-4 R20    | 6088.0                             |
|                  | 4-1 P28    | 6125.4                             |
|                  | 6-3 R63    | 6127.9                             |
|                  | 6-3 R16    | 6160.7                             |
|                  | 6-3 R17    | 6162.6                             |
|                  | 4-1 P19    | 6181.0                             |
|                  | 4-1 P18    | 6186.7                             |

**Table 4** *continued on next page*

**Table 4** (*continued*)

| Molecule         | transition              | wavenumber<br>( $\text{cm}^{-1}$ ) |
|------------------|-------------------------|------------------------------------|
|                  | 5-2 R69                 | 6187.1                             |
|                  | 4-1 P16                 | 6197.7                             |
|                  | 5-2 R64                 | 6205.6                             |
|                  | 5-2 R61                 | 6215.3                             |
|                  | 5-2 R6                  | 6215.6                             |
|                  | 4-1 R11                 | 6308.7                             |
|                  | 4-1 R19                 | 6325.2                             |
|                  | 4-1 R48                 | 6326.4                             |
|                  | 4-1 R20                 | 6326.7                             |
|                  | 3-0 R8                  | 6380.3                             |
|                  | 3-0 R53                 | 6398.3                             |
| $^{13}\text{CO}$ | 4-2 head                |                                    |
|                  | 3-1 head                |                                    |
|                  | 2-0 head                |                                    |
|                  | 3-1 R33                 | 4200.3                             |
|                  | 3-1 R69                 | 4201.0                             |
|                  | 2-0 R19                 | 4226.4                             |
|                  | 2-0 R21                 | 4230.9                             |
|                  | 2-0 R24                 | 4237.1                             |
|                  | 2-0 R35                 | 4254.5                             |
|                  | 2-0 R37                 | 4256.8                             |
|                  | 2-0 R38                 | 4257.8                             |
|                  | 2-0 R40                 | 4259.7                             |
|                  | 2-0 R41                 | 4260.5                             |
| $^{12}\text{CN}$ | 1-3 P <sub>2</sub> 38.5 | 4499.2                             |
|                  | 0-2 Q <sub>2</sub> 57.5 | 4555.0                             |
|                  | 1-3 P <sub>2</sub> 32.5 | 4584.7                             |
|                  | 1-3 P <sub>1</sub> 31.5 | 4596.3                             |
|                  | 0-2 Q <sub>1</sub> 55.5 | 4596.9                             |
|                  | 1-3 P <sub>2</sub> 31.5 | 4598.0                             |
|                  | 1-3 Q <sub>1</sub> 40.5 | 4606.5                             |
|                  | 1-3 P <sub>2</sub> 30.5 | 4611.0                             |
|                  | 0-2 Q <sub>1</sub> 54.5 | 4613.1                             |

**Table 4** *continued on next page*

**Table 4** (*continued*)

| Molecule | transition               | wavenumber<br>( $\text{cm}^{-1}$ ) |
|----------|--------------------------|------------------------------------|
|          | 1-3 P <sub>1</sub> 29.5  | 4620.7                             |
|          | 0-2 Q <sub>2</sub> 53.5  | 4621.8                             |
|          | 1-3 P <sub>2</sub> 29.5  | 4623.7                             |
|          | 0-2 Q <sub>2</sub> 52.5  | 4637.8                             |
|          | 0-2 Q <sub>2</sub> 50.5  | 4668.9                             |
|          | 1-3 P <sub>2</sub> 25.5  | 4671.8                             |
|          | 1-3 Q <sub>1</sub> 34.5  | 4672.2                             |
|          | 1-3 P <sub>2</sub> 24.5  | 4683.2                             |
|          | 0-2 Q <sub>2</sub> 49.5  | 4684.0                             |
|          | 1-3 Q <sub>2</sub> 33.5  | 4685.2                             |
|          | 1-3 P <sub>1</sub> 23.5  | 4686.4                             |
|          | 0-2 Q <sub>1</sub> 49.5  | 4689.3                             |
|          | 1-3 Q <sub>2</sub> 32.5  | 4695.4                             |
|          | 1-3 P <sub>1</sub> 22.5  | 4696.2                             |
|          | 0-2 Q <sub>2</sub> 48.5  | 4698.8                             |
|          | 1-3 Q <sub>1</sub> 31.5  | 4701.0                             |
|          | 0-1 P <sub>1</sub> 58.5  | 6308.4                             |
|          | 0-1 Q <sub>2</sub> 66.5  | 6324.4                             |
|          | 1-2 P <sub>2</sub> 42.5  | 6393.1                             |
|          | 0-1 P <sub>1</sub> 52.5  | 6437.1                             |
|          | 1-2 P <sub>2</sub> 39.5  | 6445.0                             |
|          | 0-1 Q <sub>2</sub> 60.5  | 6451.8                             |
|          | 0-1 P <sub>1</sub> 51.5  | 6457.4                             |
|          | 1-2 P <sub>2</sub> 37.5  | 6477.9                             |
| OH       | 4-2 P <sub>2f</sub> 5.5  | 6080.0                             |
|          | 2-0 P <sub>2f</sub> 15.5 | 6079.6                             |
|          | 3-1 P <sub>1f</sub> 11.5 | 6107.8                             |
|          | 3-1 P <sub>2e</sub> 10.5 | 6112.8                             |
|          | 3-1 P <sub>2f</sub> 10.5 | 6113.7                             |
|          | 2-0 P <sub>1f</sub> 14.5 | 6219.5                             |
|          | 2-0 P <sub>2e</sub> 13.5 | 6223.0                             |
|          | 2-0 P <sub>2f</sub> 13.5 | 6224.3                             |
|          | 3-1 P <sub>1e</sub> 9.5  | 6227.8                             |

**Table 4** *continued on next page*

**Table 4** (*continued*)

| Molecule | transition               | wavenumber<br>( $\text{cm}^{-1}$ ) |
|----------|--------------------------|------------------------------------|
|          | 3-1 P <sub>1e</sub> 8.5  | 6283.5                             |
|          | 3-1 P <sub>2e</sub> 6.5  | 6344.8                             |
|          | 3-1 P <sub>2f</sub> 6.5  | 6345.2                             |
|          | 3-1 P <sub>2e</sub> 5.5  | 6397.3                             |
|          | 3-1 P <sub>2f</sub> 5.5  | 6397.6                             |
|          | 2-0 P <sub>1e</sub> 11.5 | 6421.4                             |
|          | 2-0 P <sub>1f</sub> 10.5 | 6482.3                             |
|          | 2-0 P <sub>1e</sub> 10.5 | 6483.5                             |
|          | 2-0 P <sub>2e</sub> 9.5  | 6487.9                             |
|          | 2-0 P <sub>2f</sub> 9.5  | 6488.7                             |
|          | 3-1 P <sub>1f</sub> 4.5  | 6479.8                             |
| HF       | 1-0 R3                   | 4279.9                             |

**Table 5.** Elemental abundances of the M supergiant

| Element | Number of<br>lines | Abundance<br>relative to solar | Uncertainty |
|---------|--------------------|--------------------------------|-------------|
| C       | 37 <sup>a</sup>    | -0.5                           | ±0.1        |
| N       | 33                 | +0.1                           | ±0.15       |
| O       | 20                 | -0.4                           | ±0.15       |
| F       | 1                  | -0.9                           | ±0.1        |
| Na      | 2                  | -0.1                           | ±0.1        |
| Al      | 4                  | -0.2                           | ±0.1        |
| Si      | 7                  | -0.5                           | ±0.2        |
| Sc      | 6                  | +0.2                           | ±0.05       |
| Ti      | 14                 | -0.25                          | ±0.1        |
| V       | 4                  | -0.15                          | ±0.2        |
| Mn      | 1                  | +0.3                           | ±0.1        |
| Fe      | 19                 | -0.4                           | ±0.2        |

<sup>a</sup>Number of <sup>12</sup>CO lines used for the analysis. In addition, several band heads were included in the fit.

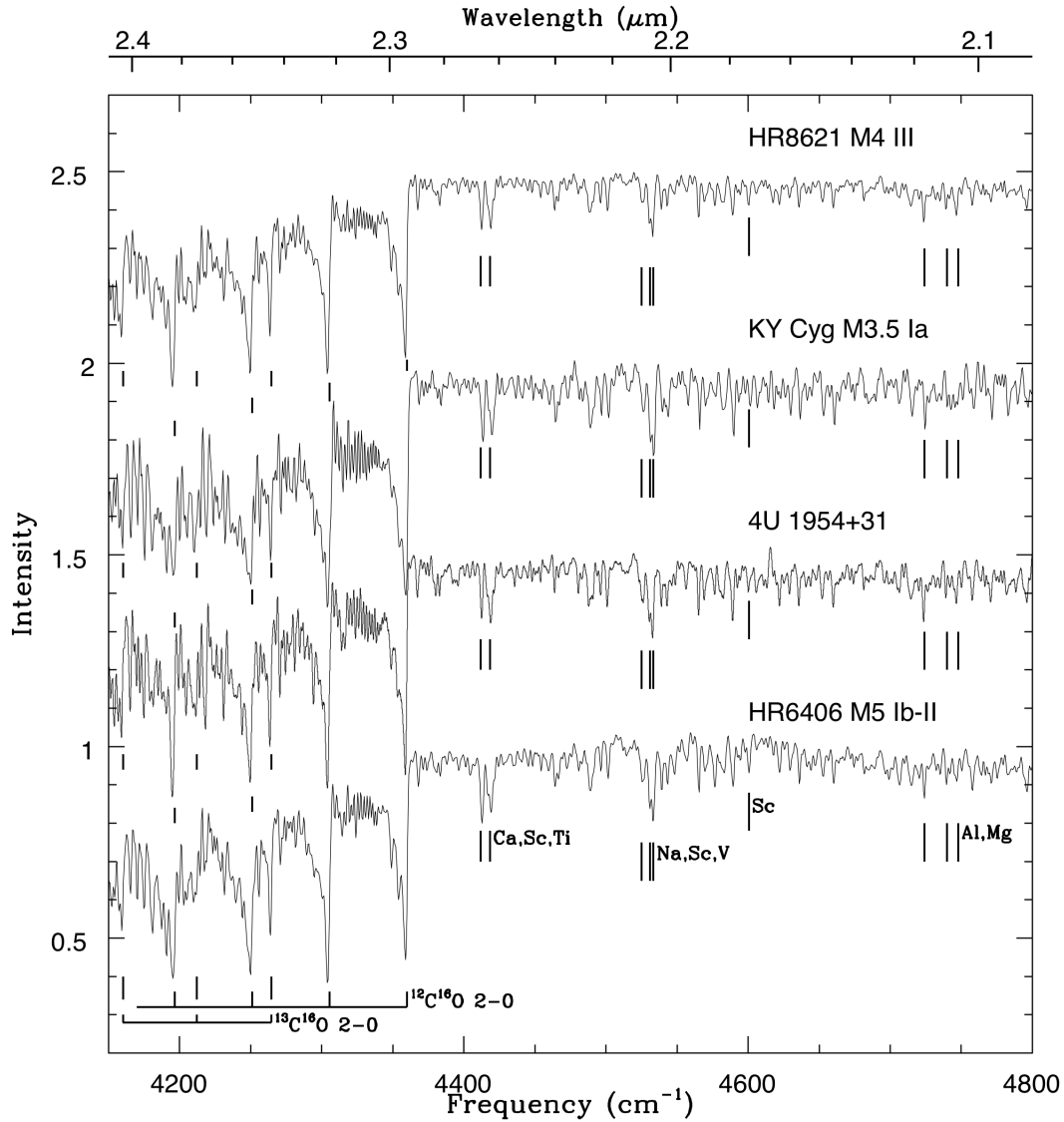


**Figure 1.** The IGRINS K band spectrum of 4U 1954+31 convolved to  $R=3000$  and compared to standard star spectra from Wallace & Hinkle (1997). The molecular and atomic lines in 4U 1954+31 are conspicuously stronger than in the M4 III spectrum (top) demonstrating that 4U 1954+31 is indeed a M supergiant. The CO bands are stronger than in the M5 Ib-II spectrum and similar to the M3.5 Ia spectrum. The Brackett  $\gamma$  emission feature at  $4616 \text{ cm}^{-1}$  in 4U 1954+31 is a reduction artifact.

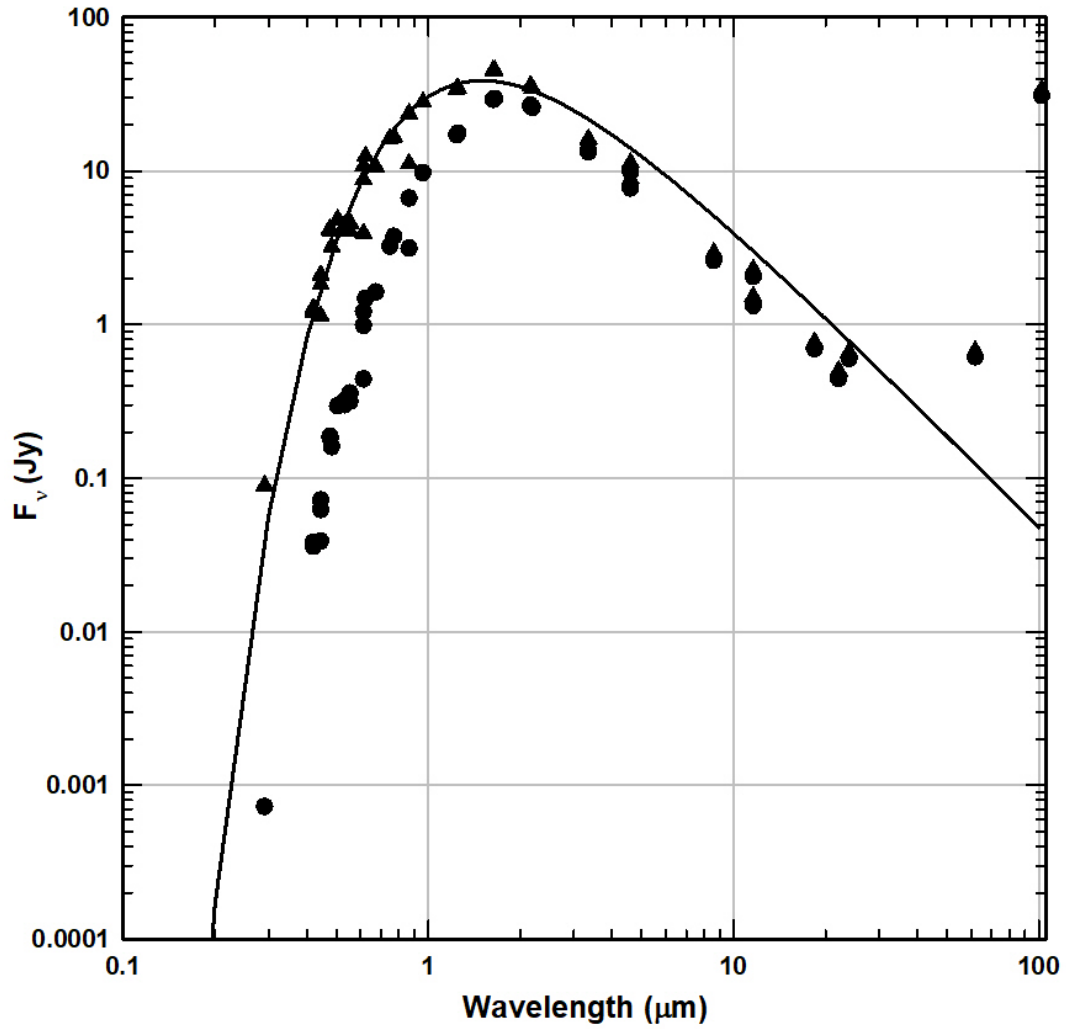


**Figure 2.** The SED for 4U 1954+31. Circles – Photometry for 4U 1954+31 taken from the VIZIER data base. Triangles – Photometry de-reddened to  $(V-K)=4$ . Line – 3400 K blackbody.

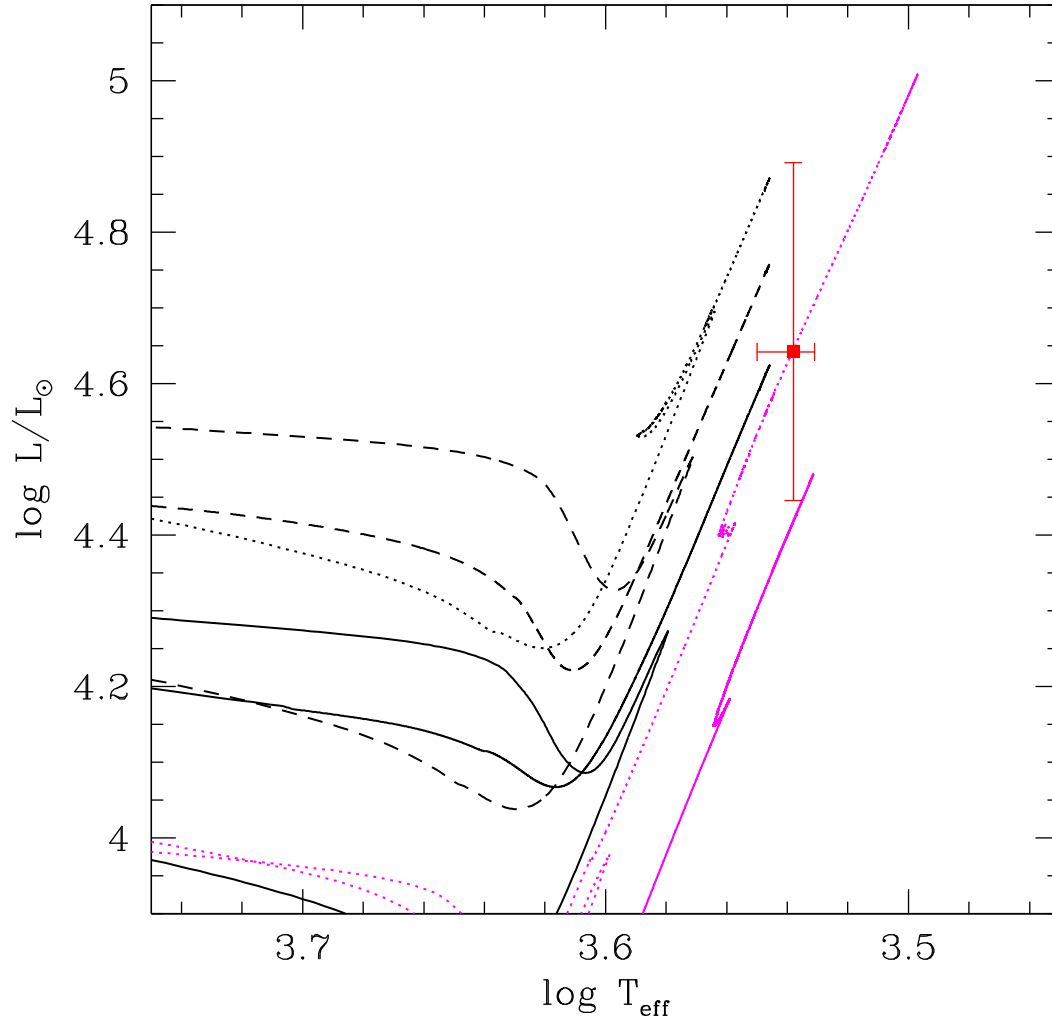


**Figure 3.** Location of the M supergiant component (red square with uncertainties shown) of the 4U 1954+31 binary on the HRD. Lines denote FuNS evolutionary tracks for  $7 M_{\odot}$  (solid magenta),  $9 M_{\odot}$  (dotted magenta),  $11 M_{\odot}$  (solid black),  $13 M_{\odot}$  (dashed black), and  $15 M_{\odot}$  (dotted black). For  $M \leq 13 M_{\odot}$  the evolutionary tracks loop to higher temperatures, beyond the 5000 K boundary of the abscissa, during the core-He burning phase.

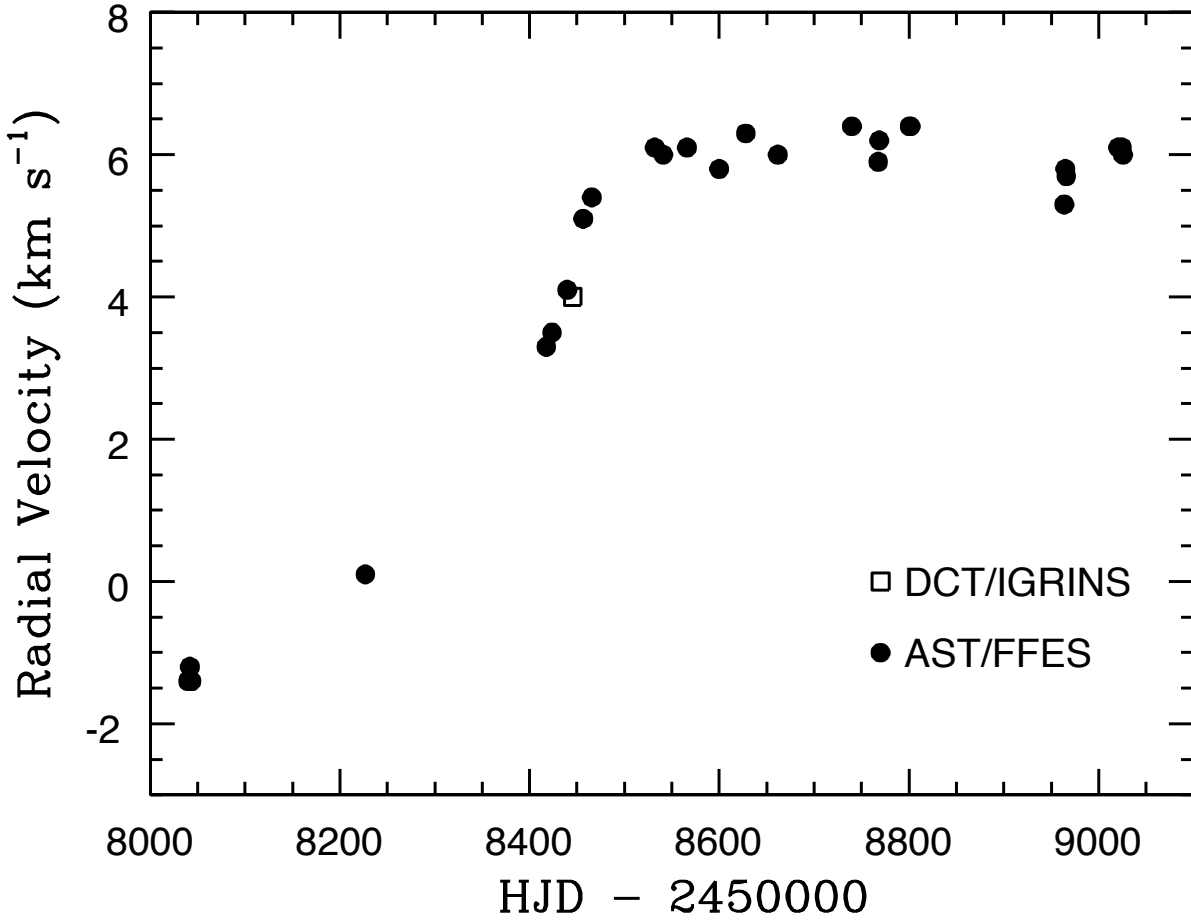


**Figure 4.** Radial velocities of the M I component of 4U 1954+31 from Table 4. The velocities span an interval of 2.7 yrs (Table 1). The period of the orbital motion is clearly much larger.